Journal of Solid State Chemistry **150,** 19–30 (2000)
doi:10.1006/jssc.1999.8541, available online at http://www.idealibrary.com on IDEAL®

Structure, Chemical Bonding, and Properties of $ZrIn_2$, $IrIn_2$, and $Ti_3Rh_2In_3$

Markus F. Zumdick,* Gregory A. Landrum,† Richard Dronskowski,† Rolf-Dieter Hoffmann,* and Rainer Pöttgen*

*Anorganisch-Chemisches Institut, Universität Münster, Wilhelm-Klemm-Strasse 8, D-48149 Münster, Germany; and
†Anorganisch-Chemisches Institut, Rheinisch-Westfälische Technische Hochschule Aachen, Professor-Pirlet-Strasse 1, D-52056 Aachen, Germany
E-mail: pottgen@uni-muenster.de; drons@HAL9000.ac.rwth-aachen.de

Received June 15, 1999; in revised form October 4, 1999; accepted October 22, 1999

DEDICATED TO PROFESSOR ARNDT SIMON ON THE OCCASION OF HIS 60TH BIRTHDAY

$ZrIn_2$, $IrIn_2$, and $Ti_3Rh_2In_3$ were prepared from the elements by reactions in sealed tantalum tubes. $ZrIn_2$ and $IrIn_2$ have previously been characterized only on the basis of X-ray powder data. Their structures were now refined from single-crystal X-ray diffractometer data: $I4_1/amd$, $a = 438.70(8)$ pm, $c = 2723.8(7)$ pm, w$R2 = 0.0308$, 561 F^2 values, 14 variables for $ZrIn_2$ ($HfGa_2$-type); $Fddd$, $a = 980.1(1)$ pm, $b = 534.67(8)$ pm, $c = 1804.9(2)$ pm, w$R2 = 0.0462$, 522 F^2 values, 17 variables for $IrIn_2$ (Mg_2Cu-type); and $P\bar{6}2m$, $a = 728.7(3)$ pm, $c = 306.7(1)$ pm, w$R = 0.0192$, 261 F^2 values, 12 variables for $Ti_3Rh_2In_3$ (ordered Th_3Pd_5-type). $ZrIn_2$ crystallizes with a superstructure of the cubic close-packing. Six different ordered fcc cells are stacked one upon each other. A group–subgroup scheme for various fcc superstructures is presented. Due to the distortions in the superstructure, the two crystallographically different indium atoms form separate networks: zig-zag chains by In1 and a square network by In2. The iridium atoms in $IrIn_2$ form infinite chains with an Ir–Ir distance of 280 pm. Each iridium atom has a square antiprismatic indium coordination. Also in $IrIn_2$ we observe two independent indium networks: the In1 atoms form a spiral-like three-dimensional network which is penetrated by planar two-dimensionally infinite layers of condensed enlongated In_6 hexagons. LMTO electronic structure calculations revealed that the In–In interactions within the In networks of $ZrIn_2$ and $IrIn_2$ are slightly stronger than those between these networks. $ZrIn_2$ and $IrIn_2$ are Pauli paramagnetic and good metallic conductors. $Ti_3Rh_2In_3$ is the first compound which adopts an ordered Th_3Pd_5-type structure. The rhodium and indium atoms form a two-dimensional $[Rh_2In_3]$ network. The distorted pentagonal prismatic channels of the $[Rh_2In_3]$ network are threaded by linear chains of titanium atoms with a Ti–Ti distance of 307 pm. According to LMTO electronic structure calculations, the strongest bonding interactions occur for the Ti–Rh contacts. Ti–Ti bonding in $Ti_3Rh_3In_3$ is compared with Ti–Ti and Hf–Hf bonding in Ti_2In_5 and Hf_2In_5, respectively, and the hexagonal close-packed structures of titanium and hafnium. © 2000 Academic Press

Key Words: **intermetallic indium compounds; crystal structure; chemical bonding; magnetism; electrical conductivity.**

INTRODUCTION

The binary indium compounds of the main group elements have been intensively investigated in the last 30 years with respect to their technologically important properties: InP, InAs, and InSb belong to the group of $A^{III}B^{V}$ semiconductors which find technical application as photo-semiconductors, IR detectors, CCD detectors, and transistors for high- and low-temperature use (1).

On the other hand, binary transition-metal indium compounds have mostly been investigated with respect to phase analytical purposes. Although about 80 binary compounds have been reported (2), only the crystal structures of Y_3In_5 (3), La_3In_5 (3), Ti_2In_5 (4), Hf_2In_5 (5), $RuIn_3$ (6), $CoIn_2$ (7), $CoIn_3$ (8), $RhIn_3$, $IrIn_3$ (8), Pt_3In_7 (9), and Cu_7In_3 (10) have been determined on the basis of single-crystal data. Even though many transition-metal indium alloys have wide technical applications, their structures are so far mostly undetermined. Ni_xIn_y alloys and $AuIn_2$ are used as surface coatings, and indium is also a minority component in many gold and gold–palladium alloys for use as dental material (11).

In combination with Sn, Pb, Ag, Au, Cd, Sb, Ga, and/or Bi, indium forms low-melting (320–370 K) alloys which are used as soft-solders or in applications such as security switches, thermostats, and sprinkler systems. Indium-plated metal surfaces show remarkable resistance against organic acids and salt-containing solutions and are in common technical use. Indium-plated ball bearings show notable erosion and abrasion resistance (1).

In the course of our systematic studies of structure–property relationships of binary transition-metal–indium compounds (4–6, 8), we examine here the crystal structures and properties of $ZrIn_2$ and $IrIn_2$. These compounds had so far only been characterized on the basis of X-ray powder data (12, 13). In the ternary system titanium–rhodium–indium we

0022-4596/00 $35.00
Copyright © 2000 by Academic Press
All rights of reproduction in any form reserved.

obtained the new compound $Ti_3Rh_2In_3$ with a peculiar crystal structure. The chemical bonding in $ZrIn_2$, $IrIn_2$, and $Ti_3Rh_2In_3$ is discussed on the basis of density-functional calculations and compared with metal–metal bonding in the binary compounds Ti_2In_5 (4) and Hf_2In_5 (5). A brief account of some of this work was presented recently at a conference (14).

EXPERIMENTAL

Starting materials for the preparation of $ZrIn_2$, $IrIn_2$, and $Ti_3Rh_2In_3$ were titanium sponge (Roth, $> 99.6\%$), zirconium sponge (Johnson Matthey, $> 99.5\%$), rhodium powder (Degussa, 200 mesh, $> 99.9\%$), iridium powder (Degussa, 200 mesh, $> 99{,}9\%$), and indium tear drops (Johnson Matthey, $> 99.9\%$). The elemental components were mixed in the ideal atomic ratios and sealed in tantalum tubes under an argon pressure of about 800 mbar. The argon was purified over molecular sieves and titanium sponge (900 K). The tantalum tubes were sealed in evacuated silica ampoules, heated for 2 days at 1320 K, annealed at 870 K for 2 more weeks, and quenched in air. The reactions resulted in agglomerated buttons which could easily be separated from the tantalum tubes. No reaction of the samples with the tantalum tubes was observed.

While $ZrIn_2$ and $IrIn_2$ could be obtained as single-phase materials via this route, the samples of $Ti_3Rh_2In_3$ had only a purity of about 60% with binary Ti_2In_5 (4) and $RhIn_3$ (8) as by-products. Therefore, we tried to prepare $Ti_3Rh_2In_3$ from the elemental components in an arc-melting furnace (15). In a first step, the titanium sponge was arc-melted under argon to obtain a compact button (about 500 mg). The rhodium powder was pressed into a small pellet ($\varnothing$ 6 mm), and in the final step the titanium button was arc-melted together with the rhodium pellet and indium tear drops in the ideal 3 : 2 : 3 atomic ratio. The melted ingot was turned over and remelted three times to ensure homogeneity. The weight loss after the melting procedures was less than 0.5%. The button was subsequently sealed in an evacuated silica tube and annealed at 670 K for 2 weeks. According to the X-ray powder pattern, this product had a content of about 90% $Ti_3Rh_2In_3$ besides small amounts of Ti_2In_5 (4).

Large needle-shaped crystals (up to 2 mm in length) of $Ti_3Rh_2In_3$ were obtained from an indium flux. For this purpose equal amounts of the binary compounds Ti_2In_5 (4) and $RhIn_3$ (8) were put in a sealed tantalum tube, heated to 1320 K, and subsequently cooled down at a rate of 50 K/day to 670 K. The needles could easily be broken off the brittle reaction product.

For a metallographic analysis, parts of the different $Ti_3Rh_2In_3$ samples were embedded in a methacrylate matrix (Struers, acryfix kit) and polished with diamond paste. These polished samples as well as the polycrystalline samples of $ZrIn_2$ and $IrIn_2$ were analyzed in a LEICA 420 I scanning electron microscope with Ti, Zr, Rh, and InAs as standards. No suitable standard was available for iridium. The EDX analyses were in agreement with the ideal compositions and no impurity elements heavier than sodium ($Z = 11$) were detected.

The possibility of a hydrogen contamination of the various $Ti_3Rh_2In_3$ samples was carefully checked by combustion analyses. The samples were burnt in an oxygen atmosphere and the resulting water potentiometrically titrated using an automated Karl-Fischer method (16). Between 50 and 200 mg of three different $Ti_3Rh_2In_3$ samples were analyzed. Within the accuracy of the method used ($\pm 3\%$), no hydrogen contamination was detected.

Guinier powder patterns of the samples were recorded after each reaction step with $CuK\alpha_1$ radiation using α-quartz ($a = 491.30$ pm, $c = 540.46$ pm) as an internal standard. The indexing of the diffraction lines was facilitated by intensity calculations (17) using the positional parameters of the refined structures. The lattice constants (Table 1) were obtained by least-squares fits of the Guinier powder data. The refined lattice constants of $ZrIn_2$ and $IrIn_2$ are in good agreement with the previously reported data by Raman and Schubert (12) and Ellner and Bhan (13).

Single-crystal intensity data were collected at room temperature by use of a four-circle diffractometer (CAD4) with graphite monochromatized $MoK\alpha$ radiation ($\lambda = 0.71073$ pm) and a scintillation counter with pulse height discrimination. The scans were performed in the $\omega/2\theta$ mode. Empirical absorption corrections were applied on the basis of ψ-scan data.

TABLE 1
Lattice Constants of $ZrIn_2$, $IrIn_2$, and $Ti_3Rh_2In_3$

Compound	Structure type	Space group	a (pm)	b (pm)	c (pm)	V (nm^3)	Ref.
$ZrIn_2$	$HfGa_2$	$I4_1/amd$	438.5	a	2723.0	0.5236	(12)
$ZrIn_2$	$HfGa_2$	$I4_1/amd$	438.70(8)	a	2723.8(7)	0.5242(2)	This work
$IrIn_2$	$CuMg_2$	$Fddd$	980.9(1)	534.9(1)	1806.0(2)	0.9476(1)	(13)
$IrIn_2$	$CuMg_2$	$Fddd$	980.1(1)	534.67(8)	1804.9(2)	0.9458(1)	This work
$Ti_3Rh_2In_3$	Th_3Pd_5	$P\bar{6}2m$	728.7(3)	a	306.7(1)	0.1410(2)	This work

Note. Standard deviations in the positions of the last significant digits are given in parentheses.

The magnetic susceptibilities of polycrystalline pieces of $ZrIn_2$ and $IrIn_2$ were determined with a SQUID magnetometer (Quantum Design, Inc.) between 4.2 and 300 K with magnetic flux densities up to 5.5 T. Resistivitiy measurements were carried out on small irregularly shaped blocks with a conventional four-probe technique. Cooling and heating curves measured between 4.2 and 300 K were identical within the error bars, as were those for different samples.

COMPUTATIONAL METHODOLOGY

The all-electron, scalar-relativistic electronic structure calculations were performed using the linear muffin-tin orbital (LMTO) method (18–21). The electronic energy was calculated via density-functional theory, replacing the many-particle problem by a self-consistent solution of the Kohn–Sham equations, using the von Barth and Hedin parameterization of the local exchange–correlation potential (22). Diagonalization and integration of the scalar-relativistic Hamiltonian in reciprocal space was performed with the help of an improved tetrahedron method (23). All calculations were checked for convergence of energies, orbital moments, and calculated crystal orbital Hamiltonian populations (COHP) values with respect to the number of k points. The basis set of short-ranged (24) atom-centered TB-LMTOs contained s–f valence functions for Zr, Ir, Rh, Hf, and In and s–d valence functions for titanium. Zr 4f, Ir 5f, Rh 4f, Hf 5f, and In 5d and 4f orbitals were included using a downfolding technique. When necessary, "empty spheres" (atomic wavefunctions without nuclei) were incorporated using an automated procedure to increase variational freedom and improve packing. Starting from atomic Hartree potentials, the electronic structure was iterated by use of the atomic-spheres approximation (ASA), employing muffin-tin spheres blown up to overlapping and volume-filling spheres, also including a combined correction term. After having reached self-consistency, charge density plots were generated by dropping any shape approximations for the potential inside the crystal. The program used was TB-LMTO 4.7 (25), run under AIX 4.2 on an IBM RS/6000 43P.

The analysis of the chemical bonding was based upon the theoretical density of states (DOS) curves, charge density plots, and COHPs (26). COHP curves are analogous to the crystal orbital overlap population (COOP) curves familiar from semiempirical extended Hückel theory (27). Both COHP and COOP plots show DOS curves which are weighted by the contributions of each crystal orbital to some measure of the strength of a given bond. In COOP analysis, that metric is the Mulliken overlap population, while in COHP analysis it is the contribution of the covalent part of a particular interaction to the total bonding energy of the crystal. All COHP curves are presented here in a format similar to COOP curves: positive values are bonding and negative ones antibonding; i.e., –COHP is plotted. Plots of DOS and COHP curves from the LMTO data were generated using "viewkel," a part of YAeHMOP (28).

RESULTS AND DISCUSSION

Syntheses

Polycrystalline samples of $ZrIn_2$, $IrIn_2$, and $Ti_3Rh_2In_3$ are light gray and stable in air over long periods of time. No decomposition whatsoever was observed after several months. Single crystals of $ZrIn_2$ and $IrIn_2$ have an irregular, ball-like shape with a dull surface. $Ti_3Rh_2In_3$ grows in the form of long needles (up to 2-mm length) which exhibit metallic luster. The surface of these needles is sometimes coated with indium.

Structure Refinements

Single crystals of $ZrIn_2$, $IrIn_2$, and $Ti_3Rh_2In_3$ were isolated from the crushed samples after the annealing procedures and then examined by Buerger precession and Weissenberg photographs to establish both symmetry and suitability for intensity data collection. A needle-shaped crystal of $Ti_3Rh_2In_3$ was oriented with the needle axis perpendicular to the X-ray beam. The $hk0$ and $hk1$ Weissenberg photographs showed hexagonal symmetry and no systematic extinctions, compatible with space groups $P6/mmm$, $P\bar{6}2m$, and $P\bar{6}m2$, of which the non-centrosymmetric group $P\bar{6}2m$ was found to be correct during the structure refinement. The precession photographs of $ZrIn_2$ (reciprocal layer hhl) and $IrIn_2$ (reciprocal layer $h0l$) showed tetragonal and orthorhombic symmetry, respectively. The systematic extinctions on these photographs and of the CAD4 data set were compatible with space groups $I4_1/amd$ ($ZrIn_2$) and $Fddd$ ($IrIn_2$). All relevant crystallographic data and experimental details of the data collections are listed in Table 2.

The starting atomic positions were deduced from automatic interpretations of direct methods with SHELXS-97 (29), and the three structures were successfully refined with anisotropic displacement parameters for all atoms using SHELXL-97 (30) (full-matrix least-squares on F^2). The three refinements readily converged to the residuals listed in Table 2. Friedel pairs were measured for $Ti_3Rh_2In_3$ to determine the correct absolute structure. Final difference Fourier syntheses were flat and revealed no significanct residual peaks. Atomic coordinates and interatomic distances are listed in Tables 3 and 4. Listings of the anisotropic displacement parameters and structure factor tables are available.[1]

[1] Details may be obtained from Fachinformationszentrum Karlsruhe, D-76344 Eggenstein-Leopoldshafen (Germany), by quoting the Registry Nos. CSD-410968 ($ZrIn_2$), CSD-410969 ($IrIn_2$), and CSD-410967 ($Ti_3Rh_2In_3$).

TABLE 2
Crystal Data and Structure Refinements for $ZrIn_2$, $IrIn_2$, and $Ti_3Rh_2In_3$

Empirical formula	$ZrIn_2$	$IrIn_2$	$Ti_3Rh_2In_3$
Molar mass (g/mol)	320.86	421.84	693.98
Space group, Z	$I4_1/amd$, 8	$Fddd$, 16	$P\bar{6}2m$, 1
Pearson symbol	$tI24$	$oF48$	$hP8$
Calculated density (g/cm^3)	8.13	11.85	8.17
Crystal size (μm^3)	$30 \times 30 \times 30$	$20 \times 20 \times 15$	$30 \times 30 \times 150$
Transmission ratio (max/min)	1.22	1.16	1.05
Absorption coefficient (mm^{-1})	20.95	75.04	21.59
$F(000)$	1104	2800	303
θ range for data collection	2°–43°	2°–35°	2°–35°
Range in hkl	$+8, \pm 8, \pm 51$	$\pm 15, \pm 8, -25 \leq l \leq 28$	$\pm 11, \pm 11, \pm 4$
Total no. of reflections	3846	3693	2871
Independent reflections	561 ($R_{int} = 0.0384$)	522 ($R_{int} = 0.0797$)	261 ($R_{int} = 0.0368$)
Reflections with $I > 2\sigma(I)$	379 ($R_{sigma} = 0.0275$)	356 ($R_{sigma} = 0.0378$)	258 ($R_{sigma} = 0.0123$)
Data/restraints/parameters	561/0/14	522/0/17	261/0/12
Goodness-of-fit on F^2	1.084	1.015	1.216
Final R indices [$I > 2\sigma(I)$]	$R1 = 0.0162$	$R1 = 0.0190$	$R1 = 0.0079$
	$wR2 = 0.0270$	$wR2 = 0.0405$	$wR2 = 0.0191$
R indices (all data)	$R1 = 0.0313$	$R1 = 0.0447$	$R1 = 0.0082$
	$wR2 = 0.0308$	$wR2 = 0.0462$	$wR2 = 0.0192$
Extinction coefficient	0.00101(5)	0.00019(1)	0.041(1)
Largest diff. peak and hole	1.61 and -1.85 e/Å^3	2.40 and -2.36 e/Å^3	0.66 and -0.51 e/Å^3

Magnetic and Electrical Properties of $ZrIn_2$ and $IrIn_2$

The temperature dependence of the magnetic susceptibilities for $ZrIn_2$ and $IrIn_2$ is shown in Fig. 1. The susceptibilities were very small and only slightly field-dependent, indicating very small quantities of ferromagnetic impurities. The 1- and 3-T data were almost identical; we have therefore plotted the 1-T data. Down to about 30 K the susceptibilities of both compounds are nearly temperature-independent with room temperature values of $+0.3(1) \times 10^{-9}$ m^3/mol ($ZrIn_2$) and $-2.3(1) \times 10^{-9}$ m^3/mol ($IrIn_2$). Below 30 K the susceptibilities show a slight increase, most likely due to very small amounts of paramagnetic impurities in the samples; however, the Guinier powder patterns showed only the reflections of $ZrIn_2$ or $IrIn_2$.

For an approximate correction for the core diamagnetism, we assume the increments of the neutral transition metals (all following values are given in units of 10^{-9} m^3/mol) of -0.97 for zirconium and -0.78 for iridium as given by Klemm in Ref. (31). For indium we use the diamagnetic susceptibility of -0.8 of the element (32). With these increments we obtain values of -2.57 and -2.38 for the core diamagnetism of $ZrIn_2$ and $IrIn_2$, respectively. Substracting these susceptibilities from the experimental data, we obtain the small, positive values of $+2.87$ ($ZrIn_2$) and $+0.08$ ($IrIn_2$) for the contribution of the conduction electrons to the Pauli paramagnetism. This is certainly a rough estimation since the diamagnetic increments, available in the literature, do not precisely match the real charge distributions. Due to the large core diamagnetism, we still observe negative susceptibilities for $IrIn_2$. Similar magnetic behavior was recently observed for $IrIn_3$ (8).

Due to the very irregular surface of the various samples, the absolute values of the specific resistivities of $ZrIn_2$ and $IrIn_2$ are somewhat inaccurate. We therefore plot the normalized electrical resistivity $R(T)/R(300\text{ K})$ in Fig. 2. The resistivities of $ZrIn_2$ and $IrIn_2$ decrease with decreasing temperature, as is usual for metallic conductors. No

TABLE 3
Atomic Coordinates and Isotropic Displacement Parameters (pm^2) for $ZrIn_2$, $IrIn_2$, and $Ti_3Rh_2In_3$

Atom	Wyckoff site	x	y	z	U_{eq}
		$ZrIn_2$ (Space Group $I4_1/amd$)			
Zr	8e	0	1/4	0.95226(1)	57(1)
In1	8e	0	1/4	0.28717(1)	68(1)
In2	8e	0	1/4	0.12558(1)	73(1)
		$IrIn_2$ (Space Group $Fddd$)			
Ir	16g	1/8	1/8	0.25501(2)	60(1)
In1	16g	1/8	1/8	0.53892(4)	83(1)
In2	16e	0.28173(7)	1/8	1/8	84(1)
		$Ti_3Rh_2In_3$ (Space Group $P\bar{6}2m$)			
Ti	3g	0.41580(9)	0	1/2	70(1)
Rh	2c	1/3	2/3	0	60(1)
In	3f	0.76250(3)	0	0	69(1)

Note. U_{eq} is defined as one-third of the trace of the orthogonalized U_{ij} tensor.

TABLE 4
Interatomic Distances (pm), Calculated with the Lattice Constants Taken from X-ray Powder Data of $ZrIn_2$, $IrIn_2$, and $Ti_3Rh_2In_3$

$ZrIn_2$		$IrIn_2$		$Ti_3Rh_2In_3$	
Zr: 2 × In2	302.9	Ir: 2 × In2	270.4	Ti: 4 × Rh	267.5
2 × In2	305.1	2 × In1	278.9	2 × In	295.5
4 × In1	311.5	2 × Ir	279.7	4 × In	304.7
2 × In1	318.8	2 × In2	280.5	2 × Ti	306.7
2 × Zr	340.2	2 × In1	285.8	4 × Ti	379.5
In1: 2 × In1	298.5	In1: 2 × Ir	278.9	Rh: 6 × Ti	267.5
4 × Zr	311.5	2 × Ir	285.8	3 × In	284.3
2 × Zr	318.8	1 × In1	310.7	2 × Rh	306.7
2 × In2	323.4	2 × In1	312.5		
2 × In2	325.7	2 × In2	337.3		
		4 × In2	345.3		
		2 × In2	370.6		
In2: 2 × Zr	302.9	In2: 2 × Ir	270.4	In: 2 × Rh	284.3
2 × Zr	305.1	2 × Ir	280.5	2 × Ti	295.5
4 × In2	310.2	1 × In2	307.2	2 × In	299.8
2 × In1	323.4	2 × In2	323.9	4 × Ti	304.7
2 × In1	325.7	2 × In1	337.3	2 × In	306.7
		4 × In1	345.3		
		2 × In1	370.6		

Note. All distances within the first coordination spheres are listed. Standard deviations are equal or less than 0.2 pm.

pronounced anomaly is detected down to 4.2 K. The room temperature values of the specific resistivities are 20 ± 5 μΩ-cm for $ZrIn_2$ and 120 ± 20 μΩ-cm for $IrIn_2$. The large error limits account for the different values obtained for several samples. At 4.2 K the resistivities have dropped to about

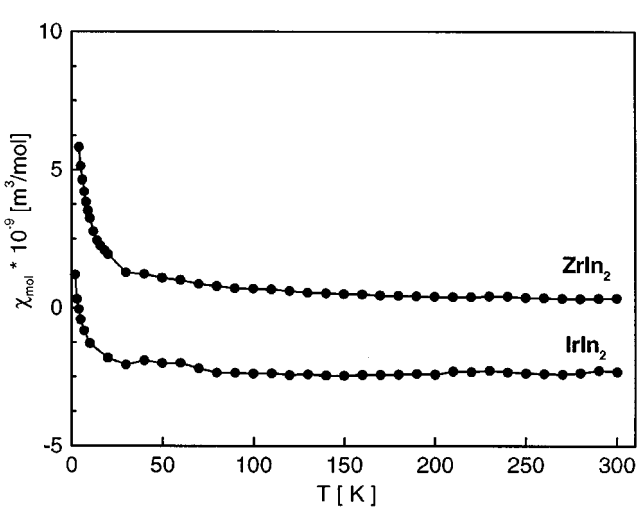

FIG. 1. Temperature dependence of the magnetic susceptibility of $ZrIn_2$ and $IrIn_2$, measured at a magnetic flux density of 1 T.

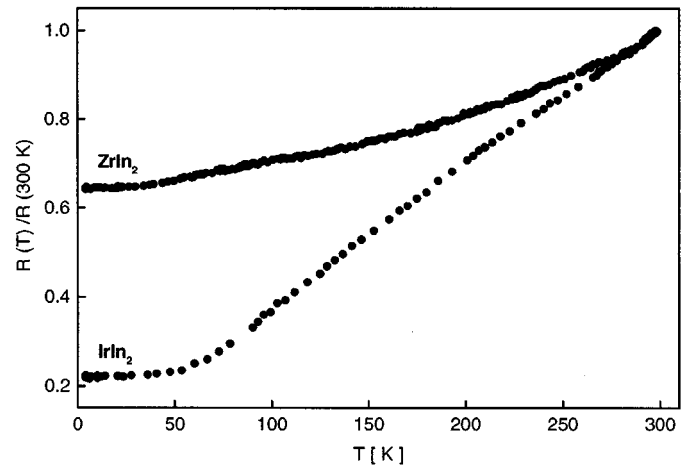

FIG. 2. Temperature dependence of the normalized specific resistivity $R(T)/R(300\,K)$ of $ZrIn_2$ and $IrIn_2$.

64% ($ZrIn_2$) and 22% ($IrIn_2$) of their room temperature values.

Crystal Chemistry and Chemical Bonding

The structure of $ZrIn_2$. Up to this point only the lattice parameters of $ZrIn_2$ have been determined (12). Raman and Schubert observed isotypism with the $HfGa_2$-type structure. The latter may be considered as a superstructure of the cubic close-packed structure where six ordered distorted fcc cells are stacked upon each other. So far, only nine compounds, i.e., $MgAl_2$, $TiAl_2$, $TiGa_2$, $ZrGa_2$, $HfGa_2$, $ZrIn_2$, $PuSn_2$, $PrPb_2$, and $PuPb_2$ (2, 33) have been reported with this peculiar atomic arrangement.

It is well known that close-packed structures can show significant distortions in an ordered state. We have therefore refined the $ZrIn_2$ structure from single-crystal X-ray data to determine the precise atomic positions. The unit cell of $ZrIn_2$ is drawn in Fig. 3. The 3 crystallographically different atoms—Zr, In1, and In2—have distorted cuboctahedral environments: Zr with 2Zr + 10In, In1 with 6Zr + 6In, and In2 with 4Zr + 8In neighbors. An inspection of the interatomic distances (Table 4) clearly illustrates the distortions present in these cuboctahedra. The Zr–Zr, Zr–In, and In–In distances from the central atom to its 12 neighbors cover a wide range: 299–340 pm.

The heavy distortions in the $ZrIn_2$ structure lead to two different networks of the two crystallographically different indium atoms. While the In1 atoms form planar zig-zag chains with an In1–In1 distance of 299 pm, the In2 atoms build a square-planar network with In2–In2 distances of 310 pm (Fig. 3). The In1–In2 distances between the networks of 323 and 325 pm are somewhat longer. All of these In–In distances, however, are shorter than the In–In

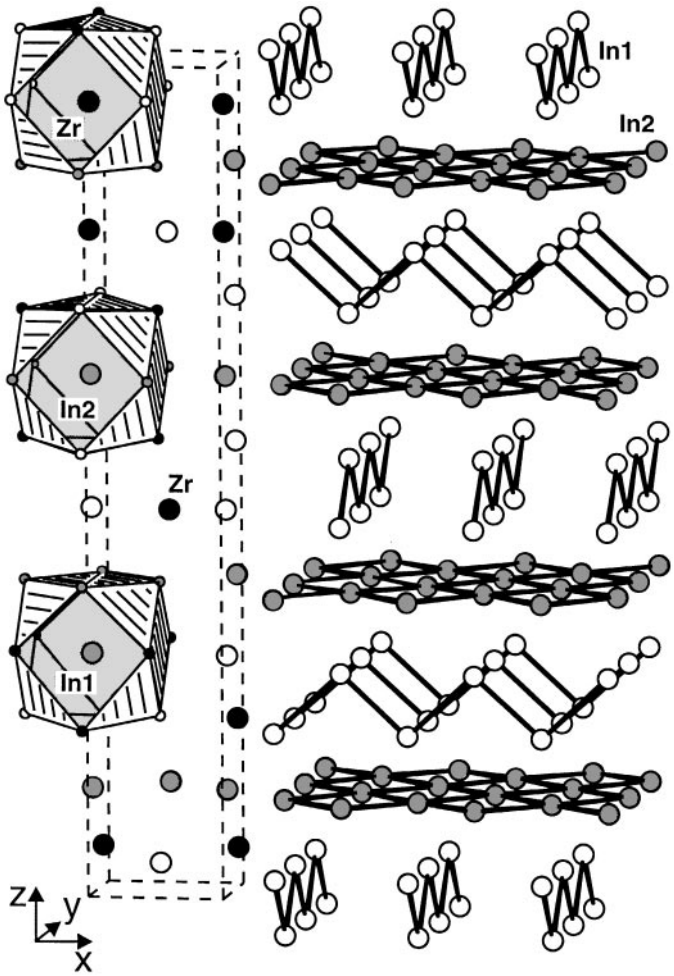

FIG. 3. Crystal structure of $ZrIn_2$. The tetragonal unit cell and the distorted cuboctahedra around the Zr, In1, and In2 atoms are shown at the left-hand side. The different networks formed by In1 and In2 are emphasized at the right-hand side.

distances in the tetragonal body-centered structure of elemental indium ($a = 325.2$ pm, $c = 494.7$ pm (34)), where each indium atom has four nearest neighbors at 325 pm and eight further neighbors at 338 pm. The average In–In distance amounts to 334 pm.

The chemical bonding in $ZrIn_2$ was investigated by LMTO band structure calculations. The DOS in the valence region has significant zirconium character with indium levels contributing from -10 eV up to the Fermi level (Fig. 4). For a more quantitative bonding analysis we now turn to the integrated crystal orbital Hamilton populations (ICOHPs) which provide a quantitative measure of the strength of the bonding. The strongest bonding interactions were found for the Zr–In2 contacts (-1.314 eV and -1.320 eV/bond), followed by the Zr–Zr contacts (-1.211 eV/bond). In–In bonding within the In1 zig-zag chains (-1.001 eV/bond) and the In2 squares (-0.796 eV/bond) is weaker. This is in agreement with the trend in the bond lengths. The Zr–Zr distances of 340 pm are only about 6% longer than those in *hcp* zirconium (321 pm average Zr–Zr distance (34)). The various Zr–In distances range from 303 to 319 pm. These are somewhat smaller than the sum of the zirconium and indium metallic radii for coordination number (CN) 12 of 327 pm (35). A quite similar bonding pattern was found recently for isotypic $ZrGa_2$ (33).

The structure of $ZrIn_2$ is closely related to the structures of the nitrides Ca_4In_2N and Sr_4In_2N (36). The nitrides may be considered as filled variants of the $HfGa_2$ structure type. With respect to $ZrIn_2$, the zirconium and the In2 positions are occupied by the calcium atoms but the In1–In1 zig-zag chains remain. The nitrogen atoms fill octahedra formed by the calcium atoms. Thus, the Ca_4In_2N structure is composed of two-dimensional layers ${}^{2}_{\infty}[NCa_2Ca_{4/2}]$ of condensed octahedra separated by the indium zig-zag chains. The In–In distances within the chains of Ca_4In_2N (316 pm) and Sr_4In_2N (332 pm) are significantly longer than those in $ZrIn_2$ (299 pm). The bonding in Ca_4In_2N was recently investigated by Miller (37) whose calculations suggested either a formulation $(4Ca)^{7+}(2In^{2-})^{4-}(N^{3-})$ with some electrons remaining on the calcium atoms or an equivalent formulation $(4Ca^{2+})^{8+}(2In^{2-})^{4-}(N^{3-})(e^-)$ indicating metallic behavior. A similar bonding situation was also recently observed for $CaAuIn_2$, where some electrons remain in calcium-centered bands (38). A simple assignment of oxidation numbers as in the case of Ca_4In_2N is certainly difficult for $ZrIn_2$.

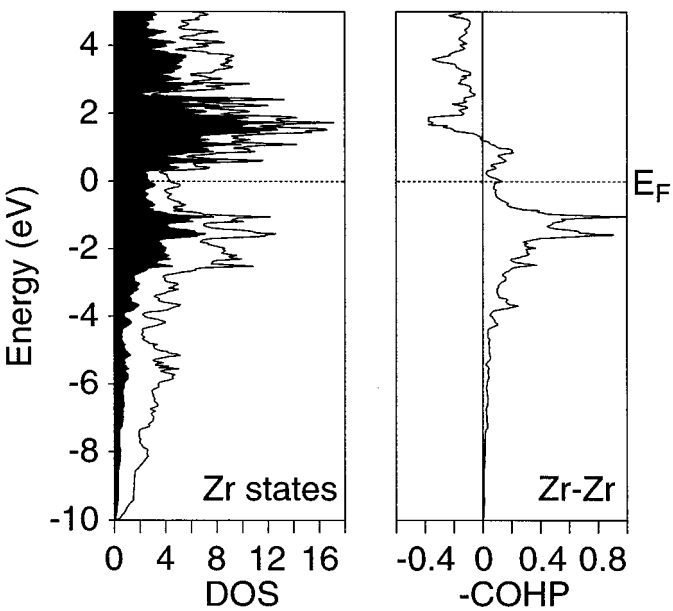

FIG. 4. Total and projected DOS for $ZrIn_2$. The Zr–Zr COHP curve is presented at the right-hand side.

Finally, it is interesting to note that the structure of $ZrIn_2$ is related to the structure of copper (ideal fcc structure) via a group–subgroup scheme (39, 40) as illustrated using the Bärnighausen formalism in Fig. 5. The group–subgroup scheme for the ordered close-packing $MoNi_4$ was already given by Bärnighausen in Ref. (39). We have now also included the structures of Cu_3Au, CuAu, $TiAl_3$, $HfGa_2$, and $ZrAl_3$ in this scheme. In those cases where filled variants exist, these structure types have also been included. In the present scheme, only those fcc superstructures where the fcc cells are stacked in the *c* direction have been considered. The crystallographic data of the listed compounds are taken from Pearson's Handbook (2).

The structure of $IrIn_2$. $IrIn_2$ has so far only been described on the basis of X-ray powder data (13, 41). Ellner and Bhan (13) correctly assigned the Mg_2Cu-type structure to this binary compound. This is fully confirmed by the present structure refinement from single-crystal X-ray data. The exact atomic positions were necessary for the evaluation of chemical bonding.

The structure of $IrIn_2$ is drawn in Fig. 6. The complex unit cell (48 atoms per cell) is presented in the left-hand part of this figure. The most striking motif is the one-dimensional, infinite chain of iridium atoms (right-hand part of Fig. 6) with Ir–Ir distances of 280 pm, only slightly larger than those in fcc iridium (272 pm (34)). Each iridium atom has a square antiprismatic coordination of eight indium atoms with Ir–In distances ranging from 270 to 286 pm. The latter compare well with the sum of Pauling's single-bond radii for iridium and indium of 276 pm (42), indicating strong Ir–In bonding. Similar Ir–In distances (265–277 pm) have recently also been observed for $IrIn_3$ (8).

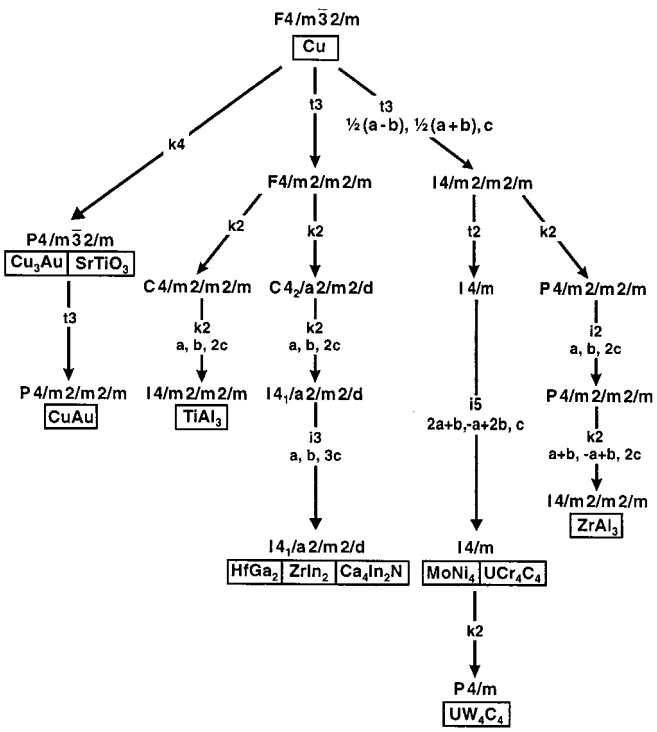

FIG. 5. Group–subgroup relationship (39, 40) for various cubic close-packed structures starting from the aristotype Cu. The indices of the *klassengleiche* (k), *translationengleiche* (t), and isomorphic (i) transitions and the unit cell transformations are given.

The DOS curve for $IrIn_2$ is presented in Fig. 7. The Ir-projected DOS indicates that the Ir *d* band is full; there is charge transfer from In to Ir. This is to be expected based upon the absolute electronegativities—5.40 eV for Ir and 3.10 eV for In (43). The Ir–Ir COHP curve, right-hand part of Fig. 7, shows that both Ir–Ir bonding and antibonding states are filled, a result which is not unusual given that this is formally a d^{10}–d^{10} interaction. What is somewhat surprising is that the integrated Ir–Ir crystal orbital Hamilton population, −1.745 eV/bond, is comparable to that in fcc iridium, − 1.730 eV/bond. The various Ir–In contacts (270–286 pm) are also significantly bonding, with ICOHP values ranging from − 1.472 to − 1.136 eV/bond.

As in the structure of $ZrIn_2$, two different interpenetrating indium networks are present. Elongated In_6 rings of In2 extend in the *xy* plane with In2–In2 distances of 307 and 324 pm, somewhat longer than those in the puckered In_6 hexagons (298 pm) of the Zintl phase $CaIn_2$ (44). Perpendicular to these planar In_6 hexagons a spiral-like three-dimensional network exists which is formed by the In1 atoms (outlined in the middle part of Fig. 6). Every other spiral has the opposite sense of rotation, indicated by small arrows in the figure. The In1–In1 distances within the spirals are 311 and 313 pm. The two indium networks penetrate each other, with somewhat greater (337 and 345 pm) In1–In2 distances. According to the corresponding ICOHP values (− 0.372 to − 0.096 eV/bond), the In–In bond strengths approximately scale with the interatomic distances: the In–In interactions within the two networks are somewhat stronger than those between them. The In–In interactions are all significantly weaker than the Ir–Ir, and Ir–In bonds.

$Ti_3Rh_2In_3$ with ordered Th_3Pd_5 type. With $Ti_3Rh_2In_3$ we have synthesized the first ternary transition-metal–rhodium–indium compound. $Ti_3Rh_2In_3$ crystallizes with a ternary ordered version of the Th_3Pd_5-type structure (45). This structure type has so far only been observed for Th_3Pd_5 (45), Th_3Pt_5 (45), Yb_3Si_5 (46, 47), and Yb_3Ge_5 (46). A projection of the $Ti_3Rh_2In_3$ structure is presented in Fig. 8. In the upper part of this drawing the trigonal prismatic titanium environment of the rhodium atoms is outlined while the $[Rh_2In_3]$ network is shown in the lower part.

The arrangement of the rhodium-centered trigonal prisms immediately brings the Fe_2P structure type (48) to mind. The structure of $Ti_3Rh_2In_3$ can indeed be derived

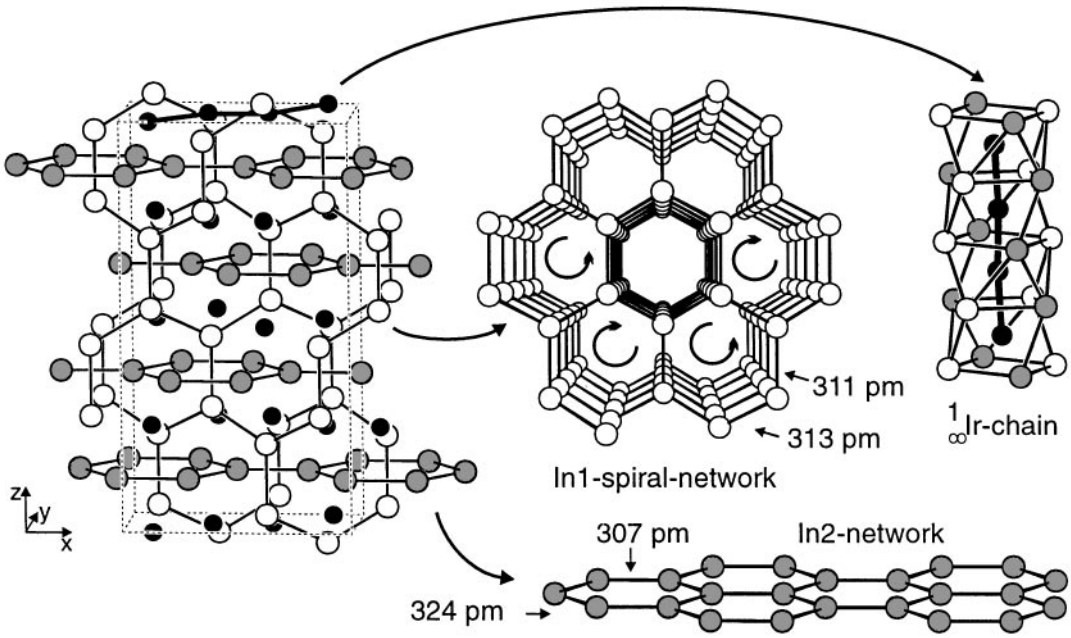

FIG. 6. Crystal structure of $IrIn_2$. The unit cell is shown in the left-hand part. The Ir, In1, and In2 atoms are drawn as black, open, and gray circles, respectively. At the middle and the right-hand side, the characteristic structural motifs, i.e., an elongated planar network of $In2_6$ hexagons, a spiral-like network of In1 atoms, and the square-antiprismatic indium environment of the iridium chains are outlined.

from the Fe_2P-type according to the formulation $Ti_3Rh_2\square In_3$, where $\square$ symbolizes the empty void at the origin of the unit cell (1*a* site of space group $P\bar{6}2m$). Due to the small size of the titanium atoms (metallic radius of 146 pm (35)), $Ti_3Rh_2In_3$ has by far the smallest c/a ratio ($c/a = 0.42$) of the Fe_2P-related compounds (49). This leads to a strong compression of the trigonal prisms of indium atoms around the origin of the unit cell, and consequently the prisms are too small to be filled with rhodium atoms. Occupancy by rhodium atoms would result in extremely short Rh–In distances of 231 pm, significantly smaller than the sum of Pauling's single-bond radii for rhodium and indium of 275 pm (42). The structure of $Ti_3Rh_2In_3$ avoids the unrealistically short Rh–In distances by leaving the indium prisms empty, giving Rh–In distances of 284 pm within the $[Rh_2In_3]$ network. With the larger rare earth atoms on the titanium positions, for example in YRhIn (50), a ZrNiAl-type (51–53) arrangement is formed where the trigonal prisms are large enough to be filled with rhodium atoms.

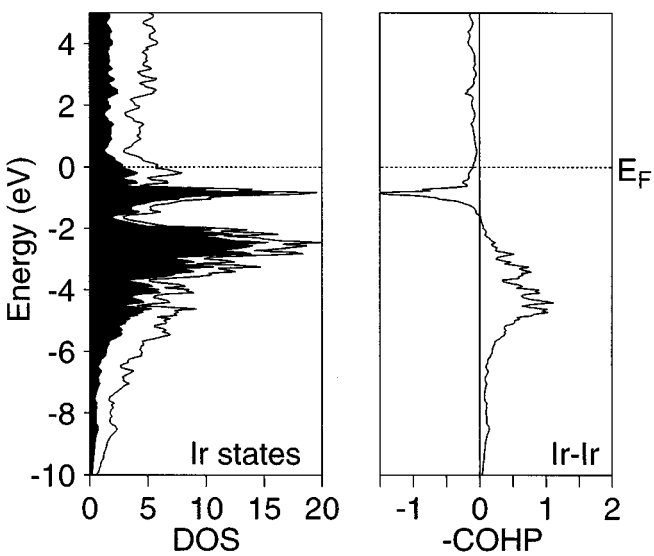

FIG. 7. Total and projected DOS for $IrIn_2$. The Ir–Ir COHP curve is presented at the right-hand side.

Apart from this purely geometric description with condensed trigonal prisms (upper part of Fig. 8), the structure of $Ti_3Rh_2In_3$ is described best by a three-dimensonal $[Rh_2In_3]$ network with large pentagonal prismatic channels which are filled with linear titanium chains (Ti–Ti distance: 307 pm). Similar pentagonal prismatic groups and linear titanium chains were also recently observed in binary Ti_2In_5 (4) with smaller Ti–Ti distances of 299 pm. In $Ti_3Rh_2In_3$ some indium positions of the pentagonal prismatic units are replaced by rhodium atoms in an ordered manner. Cutouts of the monomeric units $[TiIn_{10}]$ and $[TiRh_4In_6]$ are presented in Fig. 9. Considering the great structural similarities between Ti_2In_5 and $Ti_3Rh_2In_3$, it is certainly interesting to compare the chemical bonding in these peculiar structures.

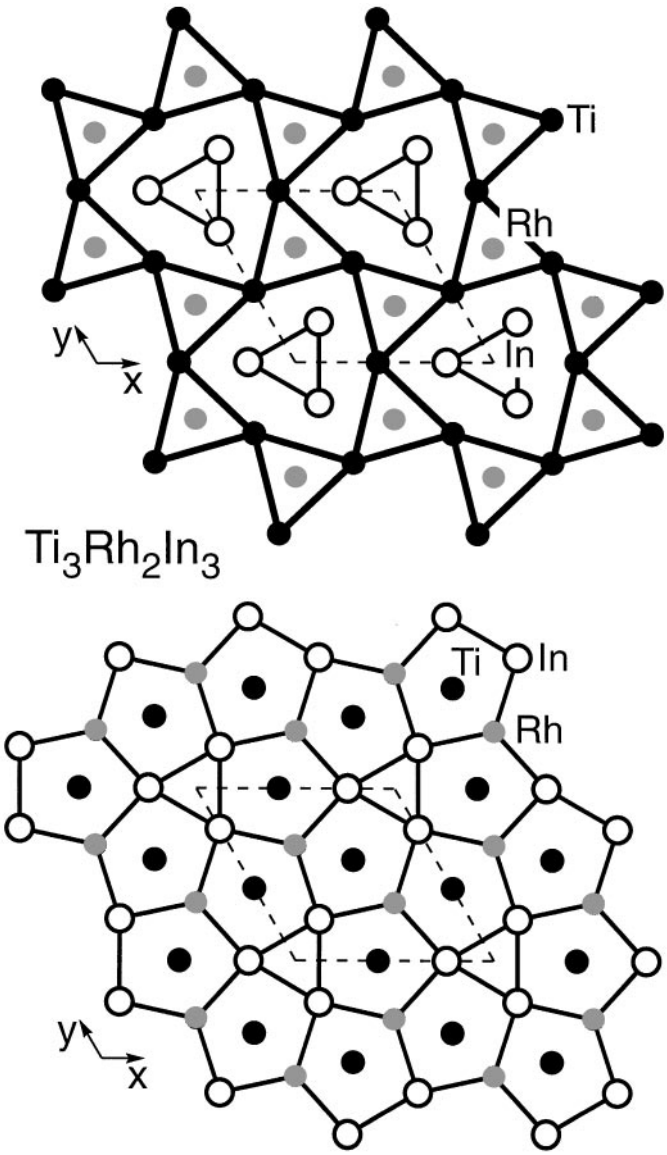

FIG. 8. Two projections of the $Ti_3Rh_2In_3$ structure along the c axis. The trigonal prismatic environment of the rhodium atoms is emphasized in the upper part and the two-dimensional $[Rh_2In_3]$ network is shown below. All atoms lie on mirror planes at $z = 0$ (thin lines) and $z = 1/2$ (thick lines). The trigonal prisms at the origin of the unit cell are unoccupied.

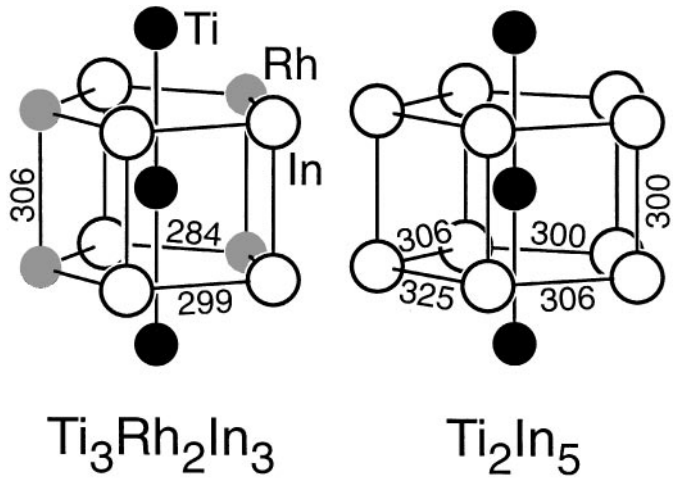

FIG. 9. Distorted pentagonal-prismatic coordination of the titanium atoms in Ti_2In_5 and $Ti_3Rh_2In_3$.

The DOS curves for both compounds are presented in Figs. 10 and 11 together with the corresponding Ti–Ti COHP curves. Comparing both DOS plots, it is readily visible that the titaniums significantly contribute to the states below the Fermi level in Ti_2In_5 (Fig. 11), while a smaller contribution is observed for $Ti_3Rh_2In_3$ (Fig. 10). The broadened block extending from -2 to -4 eV for $Ti_3Rh_2In_3$ may be ascribed to the rhodium d states. The strongest bonding interactions in $Ti_3Rh_2In_3$ were found for the Ti–Rh contacts (-1.805 eV/bond) followed by Ti–In, Rh–In, and In–In bonding. The Ti–Ti interactions within the linear chains have a significantly smaller bond strength (-0.783 eV/bond). Up to the Fermi level, only bonding Ti–Ti states are filled and a significant number of Ti–Ti bonding states remain unoccupied above E_F. This is different in binary Ti_2In_5, where almost all of the Ti–Ti bonding states lie below E_F (Fig. 11). Consequently, the strongest bonding interactions in Ti_2In_5 were found for the Ti–Ti contacts (-1.375 eV/bond). This ICOHP value is very similar to that in hcp titanium (Table 5). In $Ti_3Rh_2In_3$ the more electronegative rhodium atoms *oxidize* the Ti–Ti bonds, resulting in a reduced bond strength. Such a charge transfer

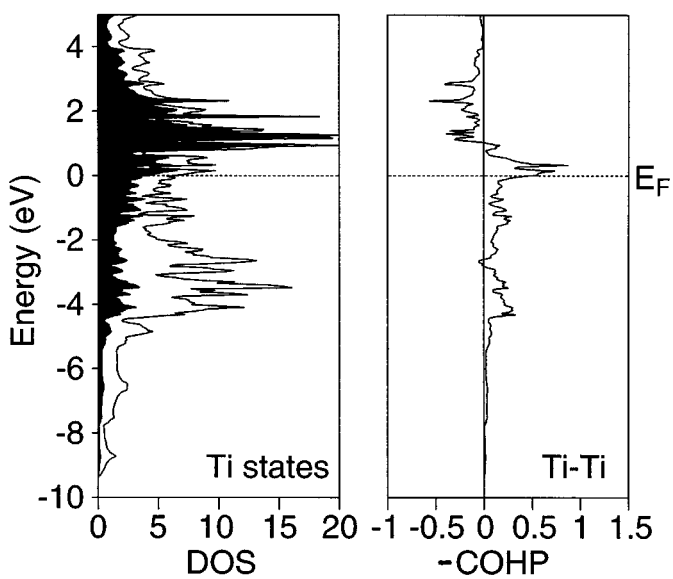

FIG. 10. Total and projected DOS for $Ti_3Rh_2In_3$. The Ti–Ti COHP curve is presented at the right-hand side.

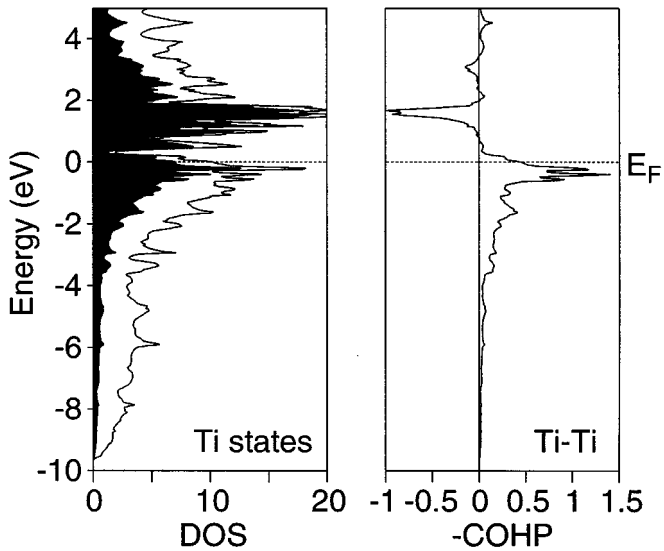

FIG. 11. Total and projected DOS for Ti_2In_5. The Ti–Ti COHP curve is presented at the right-hand side.

from the titanium and indium atoms to the rhodium atoms is again expected based upon the trend in Pearson's absolute electronegativities (Ti, 3.45 eV; Rh, 4.30 eV; and In, 3.10 eV) (43). It is finally worthwhile to note that the Rh – Rh contacts along the c axis (307 pm), with an ICOHP value of – 0.812 eV/bond, have a bond strength similar to that of the Ti–Ti contacts.

ICOHP values have also been calculated for the isotypic compound Hf_2In_5 (5) (Table 5). Here, the Hf–Hf distance within the linear chains of 306 pm is reduced by 7 pm with respect to hcp hafnium (34). The Hf–Hf ICOHP in Hf_2In_5, – 1.797 eV/bond, is significantly larger than that in hcp Hf (– 1.461 eV/bond). To determine how much of the difference in bond strengths is due to the shorter Hf–Hf bond lengths in Hf_2In_5, we carried out a calculation on Hf_2In_5 with the length of the c axis set to 313 pm (giving an Hf–Hf bond length of 313 pm). The Hf–Hf ICOHP in this expanded form of Hf_2In_5, – 1.734 eV/bond, is still stronger than that in hcp Hf.

TABLE 5
***M–M* Distances (pm) and Calculated *M–M* ICOHP (eV/Bond) Values for M_2In_5 (M = Ti, Hf), $Ti_3Rh_2In_3$, and the Elemental Structures of Ti and Hf**

Compound	$d(M–M)$	ICOHP
Ti_2In_5	299.8	– 1.375
$Ti_3Rh_2In_3$	306.7	– 0.783
hcp Ti	289.6	– 1.353
Hf_2In_5	305.7	– 1.797
hcp Hf	312.7	– 1.461

Before proceeding further, it is worthwhile to comment on the ICOHP results presented in Table 5. In the M_2In_5 structures (M = Ti, Hf), the M–M ICOHPs within the one-dimensional chains are larger than those in the corresponding elemental metals. We believe that there are two primary reasons for this seemingly strange behavior. In M_2In_5 each M atom in the chains forms only two M–M bonds, in contrast to the elemental metals where the M atoms have 12 close M–M contacts. Because the electrons in M_2In_5 must take part in fewer M–M bonds, each of those bonds is correspondingly stronger. In addition to this, calculations on the elemental structures of the early transition metals, such as Ti and Hf, reveal the expected result that there are considerable numbers of unoccupied M–M bonding states lying above E_F (54). In M_2In_5, on the other hand, all of the M–M bonding levels have been filled—the M–M bonds are as strong as they can possibly be. The dramatic effect this filling difference can have on ICOHP values is seen in the difference in the Ti–Ti ICOHPs between Ti_2In_5 and $Ti_3Rh_2In_3$: in the ternary compound, where there are less electrons on the Ti chains, the Ti–Ti bonds have not even half the strength of those in the binary compound.

Figures 12 and 13 show the valence charge density in the tetragonal respectively hexagonal xy planes at $z = 0$ of

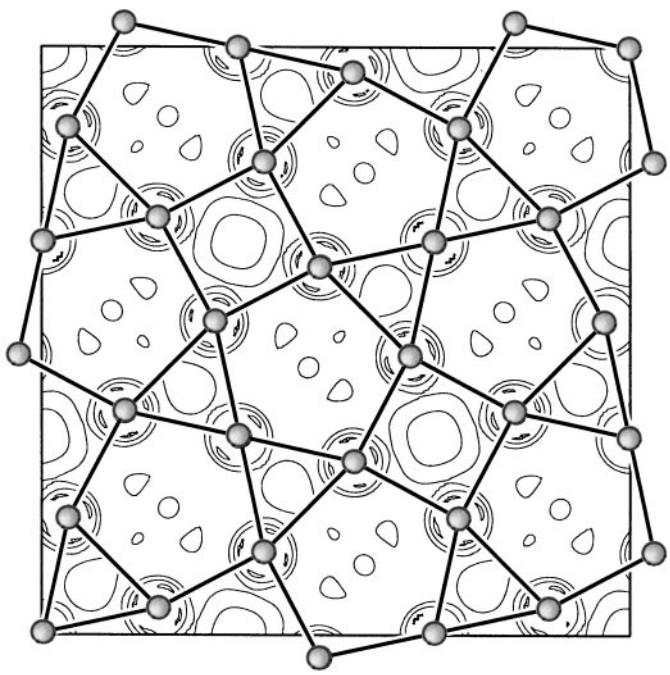

FIG. 12. Calculated valence charge density of Ti_2In_5 from first principles. A cutout of the tetragonal xy plane at $z = 0$ is shown. The steps are given in units of e/a_0^3 (a_0 is the Bohr radius of about 52.9 pm). The corresponding cutout of the structure is also shown.

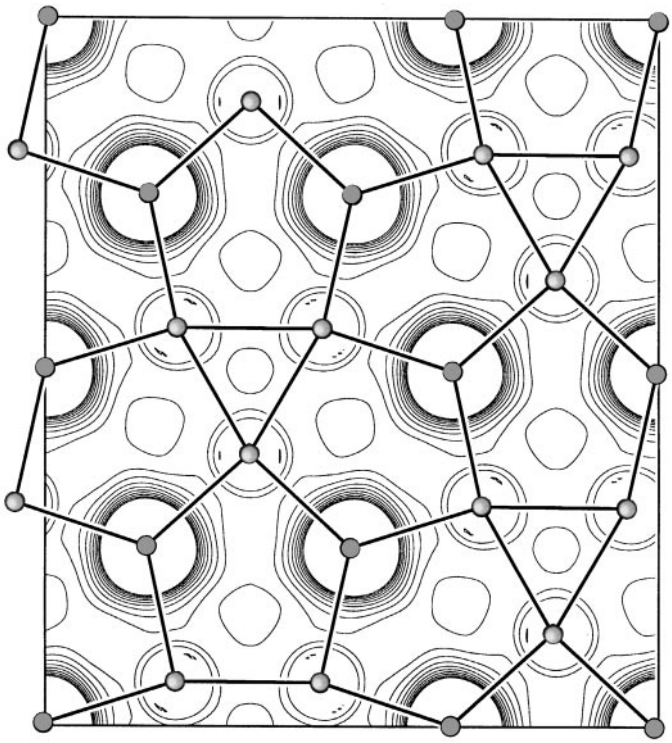

FIG. 13. Calculated valence charge density of $Ti_3Rh_2In_3$ from first principles. A cutout of the hexagonal xy plane at $z = 0$ is shown. The steps are given in units of e/a_0^3 (a_0 is the Bohr radius of about 52.9 pm). The corresponding cutout of the structure is also shown. The rhodium and indium atoms are drawn as dark gray respectively light gray circles.

Ti_2In_5 and $Ti_3Rh_2In_3$. We observe a significant residual electron density between the indium atoms in Ti_2In_5, that is, between all triangular and square units. The additional charge density, however, is not found on the direct interatomic vectors, but at positions that are shifted toward the centers of the rings, unambiguously demonstrating the multicentered nature of In–In bonding in Ti_2In_5. Also, the charge density of the Ti–Ti chains may be perceived from this figure from the residual density inside the indium pentagons, which are threaded by the titanium chains. This motif of chemical bonding is similar to our previous investigation on Hf_2In_5 (5) where the chemical bonding was investigated in more detail.

The corresponding charge density plot of $Ti_3Rh_2In_3$ (Fig. 13) is slightly different. We still observe the charge density at the centers of the In triangles resulting from the multicentered In–In bonding. Due to the charge transfer, the negatively charged rhodium atoms within the Rh_2In_3 pentagons are quite large. Each rhodium atom has a trigonal planar indium coordination with medium strength Rh–In bonding interactions (-1.067 eV/bond). Again, the electron density arising from the Ti–Ti chains which thread the pentagons is clearly visible.

CONCLUSION

The indium compounds $ZrIn_2$, $IrIn_2$, and $Ti_3Rh_2In_3$ have been prepared from the elements in sealed tantalum tubes and their structures have been investigated by X-ray diffraction techniques. $ZrIn_2$ and $IrIn_2$ have two crystallographically different indium networks with stronger In–In interactions within and weaker ones between the networks. Both compounds are metallic conductors and Pauli paramagnets. $Ti_3Rh_2In_3$ adopts a defect variant of the well-known Fe_2P-type structure. The titanium atoms form linear chains with a Ti–Ti distance of 307 pm. The distorted pentagonal prismatic coordination of the titanium atoms is similar to the structure of binary Ti_2In_5. Metal–metal bonding in the structure of $Ti_3Rh_2In_3$ is compared with metal–metal bonding in Ti_2In_5, Hf_2In_5, and the hexagonal close-packed structures of elemental titanium and hafnium, revealing significantly stronger Ti–Ti respectively Hf–Hf bonding in the binary compounds.

ACKNOWLEDGMENTS

We thank Professor W. Jeitschko for his interest and support of this work. We are also grateful to Dipl.-Ing. U. Ch. Rodewald for the diffractometer measurements, to Klaus Wagner for the EDX analysis, to Dipl.-Chem. B. Künnen for the resistivity measurements, to Dipl.-Chem. G. Kotzyba for the susceptibility measurements, to Dipl.-Ing. Roland Eger and Professor A. Simon for the combustion analyses, and to Dr. W. Gerhartz (Degussa AG) for generous gifts of rhodium and iridium powder. This work was financially supported by the Deutsche Forschungsgemeinschaft and the Fonds der Chemischen Industrie.

REFERENCES

1. L. Trueb, "Die chemischen Elemente." S. Hirzel Verlag, Stuttgart, Leipzig, 1996.
2. P. Villars and L. D. Calvert, "Pearsons Handbook of Crystallographic Data for Intermetallic Phases," 2nd ed. American Society for Metals, Materials Park, OH, 1991, and Desk Edition, 1997.
3. J.-T. Zhao and J. D. Corbett, *Inorg. Chem.* **34,** 378 (1995).
4. R. Pöttgen, *Z. Naturforsch.* **50b,** 1505 (1995).
5. R. Pöttgen and R. Dronskowski, *Chem. Eur. J.* **2,** 800 (1996).
6. R. Pöttgen, *J. Alloys Compd.* **226,** 59 (1995).
7. H. H. Stadelmaier and H. K. Manaktala, *Acta Crystallogr., Sect. B* **31,** 374 (1975).
8. R. Pöttgen, R.-D. Hoffmann, and G. Kotzyba, *Z. Anorg. Allg. Chem.* **624,** 244 (1998).
9. U. Häussermann, M. Elding-Pontén, C. Svensson, and S. Lidin, *Chem. Eur. J.* **4,** 1007 (1998).
10. S. Lidin, L. Stenberg, and M. Elding-Pontén, *J. Alloys Compd.* **255,** 221 (1997).
11. G. Beck, H.-H. Beyer, W. Gerhartz, J. Haußelt, and U. Zimmer, "Edelmetalltaschenbuch," Degussa AG, Frankfurt, 2nd ed., Auflage, Hüthig Verlag, Heidelberg, 1995.
12. A. Raman and K. Schubert, *Z. Metallkd.* **56,** 44 (1965).
13. M. Ellner and S. Bhan, *J. Less-Common Met.* **79,** P1 (1981).
14. M. F. Zumdick and R. Pöttgen, *Z. Kristallogr. Suppl.* **15,** 66 (1998).
15. R. Pöttgen, Th. Gulden, and A. Simon, *GIT-Labor-Fachzeitschrift* **43,** 133 (1999).

16. R. Eger, Hj. Mattausch, and A. Simon, *Z. Naturforsch.* **48b,** 48 (1993).
17. K. Yvon, W. Jeitschko, and E. Parthé, *J. Appl. Crystallogr.* **10,** 73 (1977).
18. O. K. Andersen, *Phys. Rev. B* **12,** 3060 (1975).
19. H. L. Skriver, "The LMTO Method." Springer-Verlag, Berlin, 1984.
20. O. K. Andersen, *in* "The Electronic Structure of Complex Systems" (W. H. Temmermann, Ed.), Plenum Press, 1984.
21. O. K. Andersen, C. Arcangeli, R. W. Tank, T. Saha-Dasgupta, G. Krier, O. Jepsen, and I. Dasgupta, *in* "Tight-Binding Approaches to Computational Materials Science," MRS Symposia Proceedings 491. MRS, Pittsburgh, 1998.
22. U. von Barth and L. Hedin, *J. Phys. C* **5,** 1629 (1972).
23. P. E. Blöchl, O. Jepsen, and O. K. Andersen, *Phys. Rev. B* **49,** 16223 (1994).
24. O. K. Andersen and O. Jepsen, *Phys. Rev. Lett.* **53,** 2571 (1984).
25. G. Krier, O. Jepsen, A. Burkhardt, and O. K. Andersen, The TB-LMTO-ASA program, version 4.7.
26. R. Dronskowski and P. E. Blöchl, *J. Phys. Chem.* **97,** 8617 (1993).
27. R. Hoffmann, "Solids and Surfaces: A Chemist's View of Bonding in Extended Structures." VCH, Weinheim, New York, 1988.
28. G. A. Landrum, "YAeHMOP-Yet Another Extended Hückel Molecular Orbital Package," version 2.0, 1997, *available at* http://overlap.chem.cornell.edu:8080/yaehmop.html.
29. G. M. Sheldrick, "SHELXS-97, Program for the Solution of Crystal Structures." University of Göttingen, Germany, 1997.
30. G. M. Sheldrick, "SHELXL-97, Program for Crystal Structure Refinement." University of Göttingen, Germany, 1997.
31. A. Weiss and H. Witte, "Magnetochemie, Grundlagen und Anwendungen." Verlag Chemie, Weinheim, 1973.
32. R. C. Weast, Ed., "Handbook of Chemistry and Physics," 58th ed. CRC Press, Palm Beach, FL, 1978.
33. Yu. Grin, U. Wedig, and H. G. von Schnering, 12th International Conference on Solid Compounds of Transition Elements, St. Malo, France, 22–25 April, 1997.
34. J. Donohue, "The Structures of the Elements." Wiley, New York, 1974.
35. E. Teatum, K. Gschneidner, Jr., and J. Waber, Report LA-2345, U.S. Department of Commerce, Washington, DC, 1960.
36. G. Cordier and S. Rönninger, *Z. Naturforsch.* **42b,** 825 (1987).
37. G. J. Miller, *in* "Chemistry, Structure, and Bonding of Zintl Phase Solids" (S. M. Kauzlarich, Ed.), Chapter 1. VCH, Weinheim, 1996.
38. R.-D. Hoffmann, R. Pöttgen, G. A. Landrum, R. Dronskowski, B. Künnen, and G. Kotzyba, *Z. Anorg. Allg. Chem.* **625,** 789 (1999).
39. H. Bärnighausen, *Commun. Math. Chem.* **9,** 139 (1980).
40. U. Müller and H. Bärnighausen, "Symmetriebeziehungen zwischen den Raumgruppen als Hilfsmittel zur straffen Darstellung von Strukturzusammenhängen in der Kristallchemie." Universität Karlsruhe, Universität Gh Kassel, 1994.
41. H. H. Stadelmaier, J. D. Schöbel, R. A. Jones, and C. A. Shumaker, *Acta Crystallogr., Sect. B* **29,** 2926 (1973).
42. L. Pauling, "The Nature of the Chemical Bond and The Structures of Molecules and Crystals." Cornell University Press, Ithaca, NY, 1960.
43. R. G. Pearson, *Inorg. Chem.* **27,** 733 (1988).
44. A. Iandelli, *Z. Anorg. Allg. Chem.* **330,** 221 (1964).
45. J. R. Thomson, *Acta Crystallogr.* **16,** 320 (1963).
46. A. Iandelli, A. Palenzona, and G. L. Olcese, *J. Less-Common Met.* **64,** 213 (1979).
47. R. Pöttgen, R.-D. Hoffmann, and D. Kußmann, *Z. Anorg. Allg. Chem.* **624,** 945 (1998).
48. S. Rundqvist and F. Jellinek, *Acta Chem. Scand.* **13,** 415 (1959).
49. M. F. Zumdick and R. Pöttgen, *Z. Kristallogr.* **214,** 90 (1999).
50. R. Ferro, R. Marazza, and G. Rambaldi, *Z. Anorg. Allg. Chem.* **409,** 219 (1974).
51. P. I. Krypyakevich, V. Ya. Markiv, and Ya. Melnyk, *Dopov. Akad. Nauk. Ukr. RSR, Ser. A*, 750 (1967).
52. A. E. Dwight, M. H. Mueller, R. A. Conner, Jr., J. W. Downey, and H. Knott, *Trans. Met. Soc. AIME* **242,** 2075 (1968).
53. M. F. Zumdick, R.-D. Hoffmann, and R. Pöttgen, *Z. Naturforsch.* **54b,** 45 (1999).
54. G. A. Landrum and R. Dronskowski, *Angew. Chem.*, in press.